A perturbation method for optimization of rigid block mechanisms in the kinematic method of limit analysis

J. P. Hambleton* and S. W. Sloan

ARC Centre of Excellence for Geotechnical Science and Engineering, The University of Newcastle, Callaghan, NSW, Australia

Abstract

Collapse mechanisms consisting of sliding rigid blocks are used widely as the basis for computing bounds on limit loads in geotechnical and structural engineering problems. While these mechanisms are conceptually straightforward to analyze, evaluating kinematically admissible velocities for a particular arrangement of blocks can be a tedious process, and optimizing the geometry of the mechanism is often prohibitively cumbersome for more than a few blocks. In this paper, we present a numerical technique for evaluating and optimizing mechanisms composed of an arbitrary number of sliding triangular blocks, assuming plane strain and homogenous, ponderable material obeying the Mohr-Coulomb yield condition. In the proposed method, coordinates defining the vertices of the blocks are treated as unknowns, and the optimal geometry is found by successively perturbing the vertex coordinates and block velocities, starting initially from a user-specified arrangement of blocks. The method is applied to three different examples related to geotechnical engineering, each of which

* Corresponding author. Address: Civil, Surveying and Environmental Engineering, University of Newcastle, EA215 University Drive, Callaghan, NSW 2308, Australia; Tel.: +61 2 4921 5893; Fax: +61 2 4921 6991
Email addresses: James.Hambleton@Newcastle.edu.au (J. P. Hambleton), Scott.Sloan@Newcastle.edu.au (S. W. Sloan).

illustrate that the approach is an efficient way to evaluate bounds that are often close to the true limit load.

Keywords: Kinematic method; Upper bound; Limit analysis; Rigid block; Optimization; Perturbation; Cone programming

1. Introduction

The kinematic method of limit analysis is a well-established technique for evaluating bounds on limit loads for engineering structures. As discussed in detail by Chen [1], the method pertains to materials that can be idealized as perfectly plastic with associated plastic flow, and it rests on constructing a kinematically admissible velocity field (i.e., collapse mechanism) in which strain rates everywhere satisfy the plastic flow rule and velocities satisfy boundary conditions. For any kinematically admissible mechanism, the limit load computed by balancing the rate of dissipation by plastic deformation to the rate of work done by external forces is a rigorous bound on the true limit load. The bound is an upper bound for loads inducing collapse and a lower bound for loads resisting collapse. Regrettably, the kinematic method has come to be known more commonly as "upper bound limit analysis," which in many instances belies the nature of the analysis and the computed bound.

The kinematic method is most often implemented in one of two forms. The first, here referred to as the "analytical method," relies on postulating and geometrically constructing an admissible collapse mechanism (e.g., [2-10]). This approach typically furnishes a closed-form expression of the limit load that includes unknown parameters characterizing the geometry of the mechanism, and the objective is then to assess the values for which the computed limit load is optimal, thereby bracketing the true limit load as closely as possible. For simplicity, it

is common to assume a mechanism consisting of sliding or rotating rigid blocks separated by transition layers of infinitesimal thickness across which the velocity is discontinuous (i.e., velocity discontinuities). In such a "rigid block mechanism," the interior angles of the blocks represent the unknown geometric parameters to be optimized. When the collapse mechanism consists of only a few rigid blocks or follows a special pattern, it is possible to evaluate the optimal geometry analytically or using straightforward numerical techniques. In general, however, the analytical method is impracticable when the number of blocks is large.

The second, purely numerical form of limit analysis is so-called finite element limit analysis (FELA). The central idea of FELA is to subdivide the entire problem domain into a number of elements over which the complete velocity field is obtained by interpolating discrete values at nodal points (e.g., [11-18]). By assigning each element a unique set of nodes, velocity discontinuities corresponding to element edges are also permitted. Whereas the velocity field in the analytical method is kinematically admissible by construction, admissibility in FELA is ensured only by introducing a large set of constraints on the otherwise arbitrary velocity field as part of the procedure for optimizing the limit load. Unlike the analytical method, the constrained optimization problem emerging in FELA can be solved using large-scale mathematical programming (e.g., linear or nonlinear programming), allowing for a virtually arbitrary number of elements. When velocities are assumed constant within elements, the velocity field in FELA reverts to a rigid block mechanism, and several studies have demonstrated the effectiveness of such an approach [19-22].

Even when continuous deformation is permitted in the collapse mechanism, the majority of plastic dissipation typically occurs along velocity discontinuities, and therefore determining their optimal locations is essential. In the analytical method, the optimization process is tantamount to finding these locations. However, the accuracy of this method is

often limited by the number of blocks that can be practically analyzed, and a generally accepted method for optimizing mechanisms with a large number of blocks in an arbitrary arrangement has yet to be established. In FELA, the need to define the placement of (potential) velocity discontinuities *a priori* is a basic shortcoming of the approach, as it is unlikely that the element edges will coincide with the optimal locations. The leading approach for overcoming this drawback is to use anisotropic mesh adaptivity, which locally refines the finite element mesh based on estimates of the velocity gradient and the Hessian matrix [23]. Resolving the optimal locations of velocity discontinuities using mesh adaptivity therefore relies on introducing a potentially large number of additional elements through the course of multiple iterations.

Two different approaches for directly optimizing the locations of velocity discontinuities in a collapse mechanism can be found in the literature, and both pertain to rigid block mechanisms. The first is known as discontinuity layout optimization (DLO) [24], and it is based on identifying the optimal connectivity of potential velocity discontinuities spanning a fixed grid of nodes [24]. The second approach rests on first evaluating an admissible collapse mechanism using standard methods of FELA and then optimizing its geometry by a series of small adjustments, or perturbations, using sequential linear programming [25], a concept first introduced by Johnson [26] for rigid-plastic analysis of concrete slabs. While both DLO and the approach based on sequential linear programming have proven to be effective in analyzing stability problems, an advantage of the latter is that it can resolve the optimal locations of velocity discontinuities anywhere in space. In DLO, velocity discontinuities must always span two nodes, and the resolution therefore depends on the grid spacing.

This paper expands on the method introduced by Milani and Lourenço [25] and presents a new computational approach for optimizing rigid block mechanisms consisting of

an arbitrary number of sliding triangular blocks. The approach utilizes large-scale mathematical programming firstly to compute admissible velocities for an initial, user-specified arrangement of blocks and then to optimize the geometry of the mechanism through a sequence of successive perturbations. As compared to the method described by Milani and Lourenço [25], key enhancements are as follows:

1. Within each perturbation step, the optimization problem is cast concisely as a second-order cone programming problem, rather than a linear programming problem.
2. The formulation includes a simple means for ensuring that mechanism remains valid within each perturbation step.
3. A strategy for progressively adjusting the magnitude of the perturbations and a corresponding stopping criterion are proposed.
4. Material self-weight, which is essential for geotechnical problems, is included.

A rudimentary version of the proposed approach, without features (2)-(4) above, was presented in an earlier conference paper by the authors [27].

The proposed formulation pertains to plane strain and material obeying the Mohr-Coulomb yield condition and, as a matter of convenience, it is assumed that the limit load induces, rather than resists, collapse. Therefore, all computed bounds are upper bounds. Extension to to the case of lower bounds on loads resisting collapse is straightforward.

In the next section, an approach for computing admissible velocities for a predefined arrangement of sliding rigid blocks is presented. In Section 3, the formulation for a fixed arrangement of blocks is adapted so that the mechanism geometry is optimized through successive perturbation. Section 4 is devoted to examples, and the penultimate section presents several observations about the approach and possible areas of future research.

2. Rigid block mechanism of fixed geometry

The starting point for the formulation is to subdivide the problem domain into a number of contiguous triangular blocks (elements). As a convention, each vertex (node) in the assembly is identified by index i, where $i = 1,2,...,N_V$, and each block is identified by index j, where $j = 1,2,...,N_B$. The Cartesian coordinates of vertex i are denoted by x_i and y_i, and components of velocity in block j are $v_{x,j}$ and $v_{y,j}$.

With the exception of edges on free boundaries, each edge in the arrangement of blocks represents a potential velocity discontinuity. Velocity discontinuities are denoted by index k, where $k = 1,2,...,N_E$, and the local quantities associated with a particular discontinuity are as shown in Fig. 1. Vertex S is the "south" vertex if the discontinuity was rotated so as to be vertical on a map, and vertex N is the "north" vertex. The blocks on either side of the discontinuity are similarly denoted by E and W, which indicate the "east" and "west" blocks. Using this convention, the following vectors containing local quantities for discontinuity k are defined

$$\mathbf{x}_k = \begin{bmatrix} x_S & y_S & x_N & y_N \end{bmatrix}^T, \quad \mathbf{v}_k = \begin{bmatrix} v_{x,E} & v_{y,E} & v_{x,W} & v_{y,W} \end{bmatrix}^T \tag{1}$$

In Eq. (1), x and y are the coordinates of the local vertices, with the subscript indicating the vertex, and v_x and v_y are the components of velocity in adjacent blocks, with the subscript indicating the block. When material on one side of the discontinuity is at rest, components of velocity on that side are simply taken as zero.

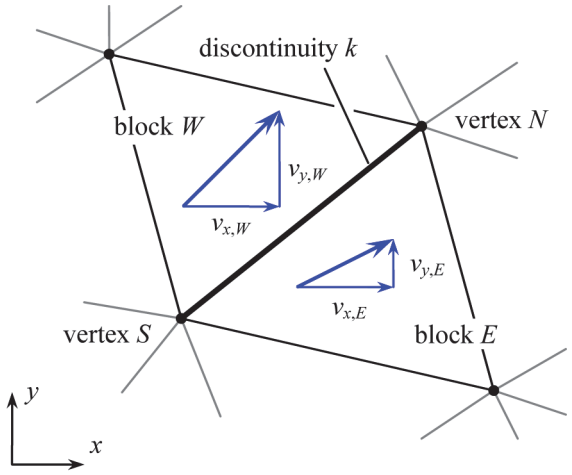

Figure 1. Local vertex and block designations for a velocity discontinuity between two adjacent blocks.

For kinematic admissibility, the following jump condition must be imposed at each velocity discontinuity (see, for instance, [1])

$$\Delta v_n = \left|\Delta v_t\right| \tan\phi \tag{2}$$

where Δv_n is the jump in components of velocity normal to the discontinuity, Δv_t is the jump in tangential components of velocity, and ϕ is the angle of internal friction. By expressing Δv_n and Δv_t in terms of v_x and v_y in adjacent blocks and performing some manipulation, the jump condition for discontinuity k can be concisely written with the aid of Eq. (1) as

$$\mathbf{x}_k^T \mathbf{P}_n \mathbf{v}_k = \left|\mathbf{x}_k^T \mathbf{P}_t \mathbf{v}_k\right| \tan\phi \tag{3}$$

where

$$\mathbf{P}_n = \begin{bmatrix} 0 & -1 & 0 & 1 \\ 1 & 0 & -1 & 0 \\ 0 & 1 & 0 & -1 \\ -1 & 0 & 1 & 0 \end{bmatrix}, \quad \mathbf{P}_t = \begin{bmatrix} -1 & 0 & 1 & 0 \\ 0 & -1 & 0 & 1 \\ 1 & 0 & -1 & 0 \\ 0 & 1 & 0 & -1 \end{bmatrix} \tag{4}$$

To derive an expression for the limit load, we first require expressions of the rate of work done by external forces and the total rate of dissipation. Assuming that unit weight is uniform and acts in the negative *y*-direction, the total rate of work done by external forces, denoted by *W*, is

$$W = \int_S \left(t_x v_x + t_y v_y \right) ds + \int_{S^*} \left(t_x^* v_x + t_y^* v_y \right) ds - \gamma \sum_{j=1}^{N_B} v_{y,j} A_j \tag{5}$$

Quantities t_x and t_y in Eq. (5) are components of a limit load represented by a surface traction that acts over the surface *S*. The tractions and the surface denoted by $(\cdot)^*$ correspond to fixed surface tractions, such as surcharge. The quantity A_j is the area of block *j*, given by

$$A_j = \frac{1}{2}\left(x_A y_B - x_A y_C + x_B y_C - x_B y_A + x_C y_A - x_C y_B \right) \tag{6}$$

where coordinates indicated by subscripts *A*, *B*, and *C* are for the local vertices of block *j* (ordered anti-clockwise so that $A_j \geq 0$).

The total rate of dissipation is obtained by summing the dissipation at individual velocity discontinuities. For a single velocity discontinuity, the rate of dissipation, *d*, is given by (see [1])

$$d = cl\left|\Delta v_t\right| \tag{7}$$

where c is cohesion and l is the length of the discontinuity. Upon expressing Δv_t in terms of $\mathbf{x}_k$ and $\mathbf{v}_k$, the dissipation at discontinuity k, denoted by d_k, can be expressed as

$$d_k = c\left|\mathbf{x}_k^T \mathbf{P}_t \mathbf{v}_k\right| \tag{8}$$

The total dissipation for the mechanism, D, is thus

$$D = \sum_{k=1}^{N_E} d_k \tag{9}$$

Upon equating the rate of work done by external forces to the total rate of dissipation ($W = D$), we find

$$\sum_{k=1}^{N_E} d_k = \int_S \left(t_x v_x + t_y v_y\right) ds + \int_{S^*} \left(t_x^* v_x + t_y^* v_y\right) ds - \gamma \sum_{j=1}^{N_B} v_{y,j} A_j \tag{10}$$

Equation (10) can be used as the basis for deriving expressions for various types of limit loads. Here we derive expressions for two specific types: (1) a pressure (i.e., zero shear stress) over part of the boundary and (2) unit weight of the material (gravity). For an applied pressure (case 1), we further assume that S is a straight line segment and that the normal component of velocity, denoted v_n, is constant over S. In this case, the first integral on the right-hand side of Eq. (10) becomes simply Pv_n, where P is the resultant force corresponding to the unknown limit load. Upon manipulation of Eq. (10), we find

$$P = \frac{1}{v_n}\left[\sum_{k=1}^{N_E} d_k - \int_{S^*}\left(t_x^* v_x + t_y^* v_y\right)ds + \gamma\sum_{j=1}^{N_B} v_{y,j} A_j\right] \tag{11}$$

Velocity v_n in Eq. (11) is a specified constant representing the kinematic boundary condition over boundary S, and it is related to the components $v_{x,j}$ and $v_{y,j}$ of the blocks whose edges belong to S through

$$v_n = v_{y,j}\cos\theta - v_{x,j}\sin\theta \tag{12}$$

where θ is the angle formed between the surface S and the x-axis (anticlockwise positive). Since we assume that P induces collapse, we require $v_n > 0$, but v_n can be otherwise selected arbitrarily.

When gravity is regarded as the limit load (case 2), the unit weight γ, a property of the material, is replaced in Eq. (10) by an unknown unit weight required to induce collapse, denoted by $\hat{\gamma}$. In this case, the first integral on the right-hand side of Eq. (10) does not appear, and the equation can be directly manipulated to find

$$\hat{\gamma} = \frac{1}{Q}\left[\int_{S^*}\left(t_x^* v_x + t_y^* v_y\right)ds - \sum_{k=1}^{N_E} d_k\right] \tag{13}$$

where

$$Q = -\sum_{j=1}^{N_B} v_{y,j} A_j \tag{14}$$

As a parallel to v_n in Eq. (11), the overall flow rate $Q > 0$ appearing in the denominator in Eq. (13) is a specified constant.

With a fixed arrangement of blocks, the only unknowns are the block velocities, and the objective is to find the velocities that minimize the limit load (Eq. (11) or (13)) subject to the following constraints: (1) the jump conditions, given for each discontinuity by Eq. (3); (2) the kinematic condition given by Eq. (12) or (14), as appropriate; and (3) problem-specific kinematic boundary conditions. By introducing two auxiliary variables for each discontinuity k, this constrained optimization problem can be represented as a so-called second-order cone programming problem (see discussion by Lyamin, *et al.* [28]). This is achieved by first replacing the quantity $\left|\mathbf{x}_k^T \mathbf{P}_t \mathbf{v}_k\right|$ in Eq. (3) with the auxiliary variable μ_k. The limit load (Eq. (11) or (13)) and the constraints from the jump conditions (Eq. (3)) then become linear with respect to the unknown velocities and unknown auxiliary variables, viz.

$$\mathbf{x}_k^T \mathbf{P}_n \mathbf{v}_k = \mu_k \tan\phi \tag{15}$$

$$P = \frac{1}{v_n}\left[c\sum_{k=1}^{N_E} \mu_k - \int_{S^*} \left(t_x^* v_x + t_y^* v_y \right) ds + \gamma \sum_{j=1}^{N_B} v_{y,j} A_j \right] \tag{16}$$

$$\hat{\gamma} = \frac{1}{Q}\left[\int_{S^*} \left(t_x^* v_x + t_y^* v_y \right) ds - c\sum_{k=1}^{N_E} \mu_k \right] \tag{17}$$

The as yet unspecified variables μ_k are then constrained by

$$\mu_k \geq \sqrt{\lambda_k^2} \tag{18}$$

where

$$\lambda_k = \mathbf{x}_k^T \mathbf{P}_t \mathbf{v}_k \tag{19}$$

To write the optimization problem in canonical form, we define a $2(N_B+N_E)\times 1$ global vector of unknowns as

$$\mathbf{x} = \left[v_{x,1}\ v_{y,1}\ v_{x,2}\ v_{y,2}\ \ldots\ v_{x,N_B}\ v_{x,N_B}\ \mu_1\ \lambda_1\ \mu_2\ \lambda_2\ \ldots\ \mu_{N_E}\ \lambda_{N_E} \right]^T \tag{20}$$

The limit load now can be written as $P = \mathbf{c}^T \mathbf{x}$ or $\hat{\gamma} = \mathbf{c}^T \mathbf{x}$, where $\mathbf{c}$ is a vector of coefficients evaluated from Eq. (16) or (17), respectively. The linear constraints of Eqs. (12), (14), (15), and (19), as applicable, can be assembled into the form $\mathbf{Ax} = \mathbf{b}$ together with other constraints required to impose kinematic boundary conditions. Upon combining these with the so-called second-order cone constraints of Eq. (18), the following second-order cone programming problem is obtained

$$\begin{aligned} &\text{minimize} && \mathbf{c}^T \mathbf{x} \\ &\text{such that} && \mathbf{Ax} = \mathbf{b} \\ & && \mu_k \geq \sqrt{\lambda_k^2} \quad \text{for } k = 1,2,\ldots,N_E \end{aligned} \tag{21}$$

It may be noted the for the velocity field to be kinematically admissible, we require $\mu_k = |\lambda_k|$ rather than the inequality in Eqs. (18) and (21). Equality is achieved, however, through the process of minimization, since the objective function is minimal when $\mu_k = |\lambda_k|$.

The optimization problem of Eq. (21) can be solved using any of a number of available software packages. For this paper, optimization was performed using the Matlab

toolbox SeDuMi [29]. By solving Eq. (21) with an assumed arrangement of blocks for which a set of admissible velocities exists, an initial collapse mechanism (i.e., velocities $v_{x,j}$ and $v_{y,j}$) and corresponding initial bound on the limit load are computed. If the assumed arrangement is selected in such a way that no set of admissible velocities exists, then Eq. (21) has no solution, and the optimization algorithm fails to converge.

3. Optimization of rigid block mechanism

With a view towards optimizing the geometry of the rigid block mechanism, the coordinates of the blocks' vertices, x_i and y_i, are now treated as unknowns to be determined as part of the solution procedure. The basic difficulty is that the jump conditions, Eqs. (15) and (19), and the expression of the limit load, Eq. (16) or (17), are nonlinear with respect to the unknown variables x_i, y_i, $v_{x,j}$, and $v_{y,j}$, which prevents the optimization problem from being cast as a standard mathematical programming problem. The remedy described in this section is to work with linear approximations rather than the exact expressions, a concept first proposed by Johnson [26] for rigid-plastic analysis of concrete slabs. These linear equations are then employed to perturb the known vertex coordinates and block velocities via optimization. By repeating this perturbation procedure a number of times, while each time updating the point about which linearization is performed, the overall geometry of the collapse mechanism is optimized. Throughout the remainder of the paper, the vertex coordinates and block velocities computed in any given perturbation step are denoted by x_i^m, y_i^m, $v_{x,j}^m$, and $v_{y,j}^m$ (m = 1,2,…), and m = 0 denotes initial quantities corresponding to the predefined arrangement of blocks used as a starting guess.

3.1. Derivation of perturbation equations

The quantity $\mathbf{x}_k^T \mathbf{P}_n \mathbf{v}_k$ in Eq. (15) can be approximated in each perturbation step using the first-order Taylor expansion

$$\mathbf{x}_{k,m}^T \mathbf{P}_n \mathbf{v}_{k,m} \approx -\mathbf{v}_{k,m-1}^T \mathbf{P}_n \mathbf{x}_{k,m} + \mathbf{x}_{k,m-1}^T \mathbf{P}_n \mathbf{v}_{k,m} - \mathbf{x}_{k,m-1}^T \mathbf{P}_n \mathbf{v}_{k,m-1} \tag{22}$$

where $\mathbf{x}_{k,m}$ and $\mathbf{v}_{k,m}$ contain unknown coordinates and velocities (x_i^m , y_i^m , $v_{x,j}^m$, and $v_{y,j}^m$) and $\mathbf{x}_{k,m\text{-}1}$ and $\mathbf{v}_{k,m\text{-}1}$ contain the known quantities from the previous perturbation step or the initial mechanism. Similarly, quantity $\mathbf{x}_k^T \mathbf{P}_n \mathbf{v}_k$ in Eq. (19) can be approximated as

$$\mathbf{x}_{k,m}^T \mathbf{P}_t \mathbf{v}_{k,m} \approx \mathbf{v}_{k,m-1}^T \mathbf{P}_t \mathbf{x}_{k,m} + \mathbf{x}_{k,m-1}^T \mathbf{P}_t \mathbf{v}_{k,m} - \mathbf{x}_{k,m-1}^T \mathbf{P}_t \mathbf{v}_{k,m-1} \tag{23}$$

Using Eqs. (22) and (23), the constraints derived from the jump conditions, Eqs. (15) and (19), become

$$-\mathbf{v}_{k,m-1}^T \mathbf{P}_n \mathbf{x}_{k,m} + \mathbf{x}_{k,m-1}^T \mathbf{P}_n \mathbf{v}_{k,m} - \mathbf{x}_{k,m-1}^T \mathbf{P}_n \mathbf{v}_{k,m-1} = \mu_k^m \tan\phi \tag{24}$$

$$\lambda_k^m = \mathbf{v}_{k,m-1}^T \mathbf{P}_t \mathbf{x}_{k,m} + \mathbf{x}_{k,m-1}^T \mathbf{P}_t \mathbf{v}_{k,m} - \mathbf{x}_{k,m-1}^T \mathbf{P}_t \mathbf{v}_{k,m-1} \tag{24}$$

where μ_k^m and λ_k^m are the counterparts of μ_k and λ_k from Section 2 for step m. A first-order Taylor expansion of the nonlinear term $v_{y,j}A_j$ appearing in Eqs. (14) and (16) gives

$$v_{y,j}^{m} A_j^{m} \approx \beta_j^{m} \tag{24}$$

where A_j^m is the area of block j for step m and

$$\begin{aligned}\beta_j^m = &\frac{1}{2} v_{y,j}^{m-1}\left(x_A^m y_B^{m-1} - x_A^m y_C^{m-1} + x_B^m y_C^{m-1} - x_B^m y_A^{m-1} + x_C^m y_A^{m-1} - x_C^m y_B^{m-1}\right) \\ &+ \frac{1}{2} v_{y,j}^{m-1}\left(x_A^{m-1} y_B^m - x_A^{m-1} y_C^m + x_B^{m-1} y_C^m - x_B^{m-1} y_A^m + x_C^{m-1} y_A^m - x_C^{m-1} y_B^m\right) \\ &+ v_{y,j}^m A_j^{m-1} - 2 v_{y,j}^{m-1} A_j^{m-1}\end{aligned} \tag{24}$$

For the case of a limit load in the form of an applied pressure, substitution of Eq. (24) into Eq. (16) gives the following definition of the limit load, which is now linear with respect to the unknowns

$$P = \frac{1}{v_n}\left[c\sum_{k=1}^{N_E} \mu_k^m - \int_{S^*}\left(t_x^* v_x^m + t_y^* v_y^m\right) ds + \gamma \sum_{j=1}^{N_B} \beta_j^m \right] \tag{25}$$

where (cf. Eq. (12))

$$v_n = v_{y,j}^m \cos\theta - v_{x,j}^m \sin\theta \tag{26}$$

When collapse is induced by unit weight, the linearized expression of the limit load becomes

$$\hat{\gamma} = \frac{1}{Q}\left[\int_{S^*}\left(t_x^* v_x^m + t_y^* v_y^m\right) ds - c\sum_{k=1}^{N_E} \mu_k^m \right] \tag{27}$$

where (cf. Eq. (14))

$$Q = -\sum_{j=1}^{N_B} \beta_j^m \tag{28}$$

With the aid Eqs. (24)-(28), we may now formulate an optimization problem similar to Eq. (21) aimed at improving the computed bound by adjusting coordinates and velocities for the mechanism. It is clear, however, that the vertices of the blocks cannot be adjusted arbitrarily, as blocks may invert (i.e. $A_j^m < 0$) and invalidate the mechanism. It is therefore necessary to introduce constraints on the perturbed vertex coordinates to ensure $A_j^m \geq 0$ for all blocks. We therefore introduce the following radial constraints on the perturbed coordinates of vertices (x_i^m and y_i^m)

$$\rho_i^m \geq \sqrt{\left(\Delta x_i^m\right)^2 + \left(\Delta y_i^m\right)^2} \tag{29}$$

where ρ_i^m is the specified constraint radius for vertex *i* in step *m* and

$$\Delta x_i^m = x_i^m - x_i^{m-1} \tag{30}$$

$$\Delta y_i^m = y_i^m - y_i^{m-1} \tag{31}$$

In Appendix A, we present a formula for assessing an upper limit on ρ_i^m, denoted by $\left(\rho_i^m\right)_{\max}$, that guarantees the mechanism will remain valid in each perturbation step (see Eq. (37)).

As in Section 2, Equations (24)-(31) can be assembled into the canonical form of a second-order cone programming problem as follows

$$\begin{aligned} &\text{minimize} && \mathbf{c}_p^T \mathbf{x}_p \\ &\text{such that} && \mathbf{A}_p \mathbf{x}_p = \mathbf{b}_p \\ & && \rho_i^m \geq \sqrt{\left(\Delta x_i^m\right)^2 + \left(\Delta y_i^m\right)^2} \quad \text{for } i = 1, 2, \ldots, N_V \\ & && \mu_k^m \geq \sqrt{\left(\lambda_k^m\right)^2} \quad \text{for } k = 1, 2, \ldots, N_E \end{aligned} \tag{32}$$

In Eq. (32), $\mathbf{x}_p$ is now a $(5N_V+3N_B+2N_E)\times 1$ global vector of unknowns, much like Eq. (20), whose entries consist of the variables of interest, x_i^m, y_i^m, $v_{x,j}^m$, and $v_{y,j}^m$, as well as the auxiliary variables μ_k^m, λ_k^m, Δx_i^m, Δy_i^m, and β_j^m. The vector $\mathbf{c}_p$ is determined by the coefficients in either Eq. (25) or (27), depending on the definition of the limit load. The matrix $\mathbf{A}_p$ and vector $\mathbf{b}_p$ are obtained by assembling the coefficients and constants from Eqs. (24), (24), (24), (30), and (31) together with Eq. (26) or (28) as applicable. Arrays $\mathbf{A}_p$ and $\mathbf{b}_p$ also include kinematic boundary conditions and constraints that fix the position of certain vertices (e.g., vertices on boundaries) as required for each particular problem. Upon assembling $\mathbf{c}_p$, $\mathbf{A}_p$, $\mathbf{b}_p$, Eq. (32) can be solved using the same optimization algorithm as for Eq. (21), and the outputs are the perturbed coordinates of the blocks' vertices, estimates of the velocities for each block, and an estimate of the limit load.

3.2. Iterative perturbation procedure

The perturbed collapse mechanism evaluated from Eq. (32) does not provide a rigorous bound on the true limit load, since the jump conditions and equations for the limit load are approximate. It can be observed, however, that errors in the linearized expressions decrease as the constraint radii ρ_i^m are reduced. In fact, in the limit $\rho_i^m = 0$, it follows that $x_i^m = x_i^{m-1}$ and $y_i^m = y_i^{m-1}$, and the exact expressions of the limit load and jump conditions are recovered in Eqs. (22), (23), and (24). An iterative procedure that reduces the radii ρ_i^m as the number of perturbation steps increases (i.e., $\rho_i^m \to 0$ as $m \to \infty$) therefore provides a rigorous upper bound on the limit load within specified numerical tolerances. Also, as pointed out by Johnson [26], solution of the linearized optimization problem does not determine the magnitude of the perturbation needed to arrive at the optimal configuration, and without some means of reducing ρ_i^m, the mechanism will oscillate about the optimum rather than converge towards it.

The best procedure for progressively adjusting the magnitude of successive perturbations is unknown, and little can be stated with any generality on account of the problem-specific nature of the underlying nonlinear optimization problem. In the formulation of Milani and Lourenço [25], perturbations of fixed but small magnitude were apparently used in each of their analyses, and the authors do not discuss convergence criteria. Johnson [26] proposed an *ad hoc* method in which the constraint on each unknown variable was reduced if an oscillation over the three previous steps was detected.

The procedure proposed in this paper resembles the one utilized by Johnson [26], and it rests on reducing ρ_i^m when an oscillation in the position of vertex i is detected. As

illustrated in Fig. 2, the central idea is to regard a vertex that moves progressively further away from its former positions as "improving" in its position (Fig. 2a), while regarding a vertex that displaces back to the neighborhood of a former position as "converging" (Fig. 2b). The position of a vertex is said to be converging after step *m* if the vertex is at a distance of ρ_i^m or less from its position two steps prior (Fig. 2b). For vertices satisfying this criterion, the radius in the following step, ρ_i^{m+1}, is reduced by a factor of one half. For vertices with improving positions, the radius is held constant so as to make maximal gains towards optimizing the mechanism. Overall, the process by which the radii are reduced is represented mathematically as

$$\rho_i^{m+1} = \begin{cases} \dfrac{\rho_i^m}{2} & \text{if} \quad \sqrt{\left(x_i^m - x_i^{m-2}\right)^2 + \left(y_i^m - y_i^{m-2}\right)^2} < \rho_i^m \\ \rho_i^m & \text{if} \quad \sqrt{\left(x_i^m - x_i^{m-2}\right)^2 + \left(y_i^m - y_i^{m-2}\right)^2} \geq \rho_i^m \end{cases} \tag{33}$$

To ensure the mechanism remains valid, ρ_i^{m+1} is always taken as the smaller of the value computed from Eq. (33) and $\left(\rho_i^m\right)_{\max}$, where $\left(\rho_i^m\right)_{\max}$ is given by Eq. (37).

The natural stopping criterion following from Eq. (33) is

$$\rho_i^m \leq \varepsilon \ \forall \ i = 1, 2, \ldots, N_V \tag{33}$$

where ε is a specified tolerance. The final estimate of the limit load will be a rigorous upper bound within the tolerance ε, as well as the tolerances used in numerically solving the second-order cone programming problem given by Eq. (32).

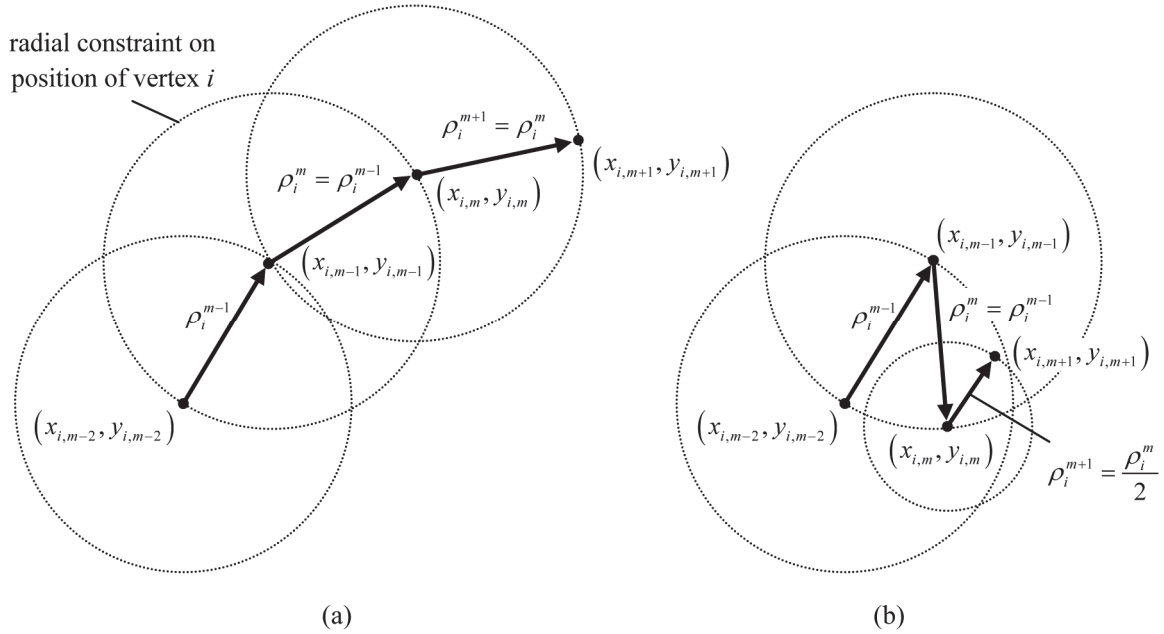

Figure 2. Evolution of radial constraint on the position of a vertex after successive perturbations: (a) constant constraint for improving position; (b) reduction in constraint for converging position.

As the perturbation process proceeds, it is possible that some blocks become severely reduced in size (i.e., $A_j^m \approx 0$). These reduced blocks can diminish the effectiveness of the perturbation process by causing the maximum constraint radii $\left(\rho_i^m\right)_{\max}$ to be become prematurely small, thus hampering improvements to the mechanism's geometry. In Appendix B, we present a simple algorithm for detecting and deleting reduced blocks. This algorithm was utilized for all examples considered in this paper. It may be noted that Milani and Lourenço [25] included a similar block deletion procedure. In their formulation, however, blocks were deleted to correct invalid geometries resulting from block inversions rather than to improve the performance of the method.

3.3. Summary of perturbation method

The full procedure for analyzing a stability problem using the proposed method can be summarized in the following steps:

1. Define an initial arrangement of blocks in terms of x_i^0 and y_i^0, and input tolerance ε and initial constraint radii, $\rho_i^1 \le \left(\rho_i^1\right)_{\max}$.
2. Assemble arrays **c**, **A**, and **b** using Eqs. (12), (14)-(17), and (19) as applicable. Introduce kinematic boundary conditions via **A** and **b**.
3. Solve the second-order cone programming problem of Eq. (21) for the vector of unknowns **x** containing velocities for the initial block assembly ($v_{x,j}^0$ and $v_{y,j}^0$).
4. Assemble arrays $\mathbf{c}_p$, $\mathbf{A}_p$, and $\mathbf{b}_p$ from Eqs. (24), (24), (24)-(28), (30), and (31) as applicable. Introduce kinematic boundary conditions and position constraints for vertices on boundaries via $\mathbf{A}_p$ and $\mathbf{b}_p$.
5. Solve the second-order cone programming problem of Eq. (32) for the vector of unknowns $\mathbf{x}_p$ containing perturbed coordinates and velocities (x_i^m, y_i^m, $v_{x,j}^m$, and $v_{y,j}^m$).
6. Detect and delete any reduced blocks following the strategy described in Appendix *B*. If a block is deleted, set $\rho_i^m = \left(\rho_i^m\right)_{\max} \ \forall \ i = 1, 2, \ldots, N_V$, where $\left(\rho_i^m\right)_{\max}$ is evaluated using Eq. (37).
7. Update ρ_i^m according to Eq. (33). If $\rho_i^m > \left(\rho_i^m\right)_{\max}$, set $\rho_i^m = \left(\rho_i^m\right)_{\max}$.
8. Repeat steps (4)-(7) until $\rho_i^m \le \varepsilon \ \forall \ i = 1, 2, \ldots, N_V$.

4. Examples

4.1. Smooth retaining wall

As a first example, the perturbation method is used to analyze a smooth, rigid retaining wall of height h translating into purely frictional soil (c = 0) with ϕ = 35º. This simple example, for which the true limit load is well known, is chosen to explore the influence of the initial arrangement of blocks, the initial constraint radii ρ_i^1, the total number of blocks N_B, and the tolerance ε on the final results. Figure 3 shows the three different initial block arrangements used as starting guesses. As shown, the blocks' vertices lie along a parabola, and each arrangement is differentiated by a different value of the parameter ξ.

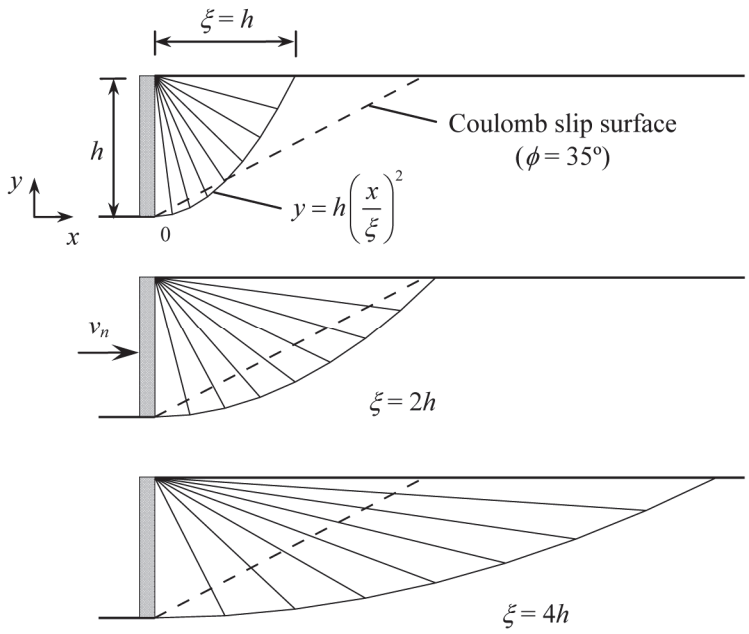

Figure 3. A smooth rigid retaining wall with various choices for the initial block arrangement.

Figures 4 and 5 show the collapse mechanism at various perturbation steps for the cases $\xi = h$ and $\xi = 4h$, respectively, based on computations with $N_B = 8$ and $\rho_i^1 = 0.04h$. Despite the difference in the initial arrangement of blocks, the mechanism converges to that predicted by Coulomb's theory of earth pressure in both cases. With $\xi = 4h$, it is seen that the blocks at the free surface tend to reduce in size during successive perturbation, but by using the algorithm described in Appendix B, these blocks are systematically detected and deleted.

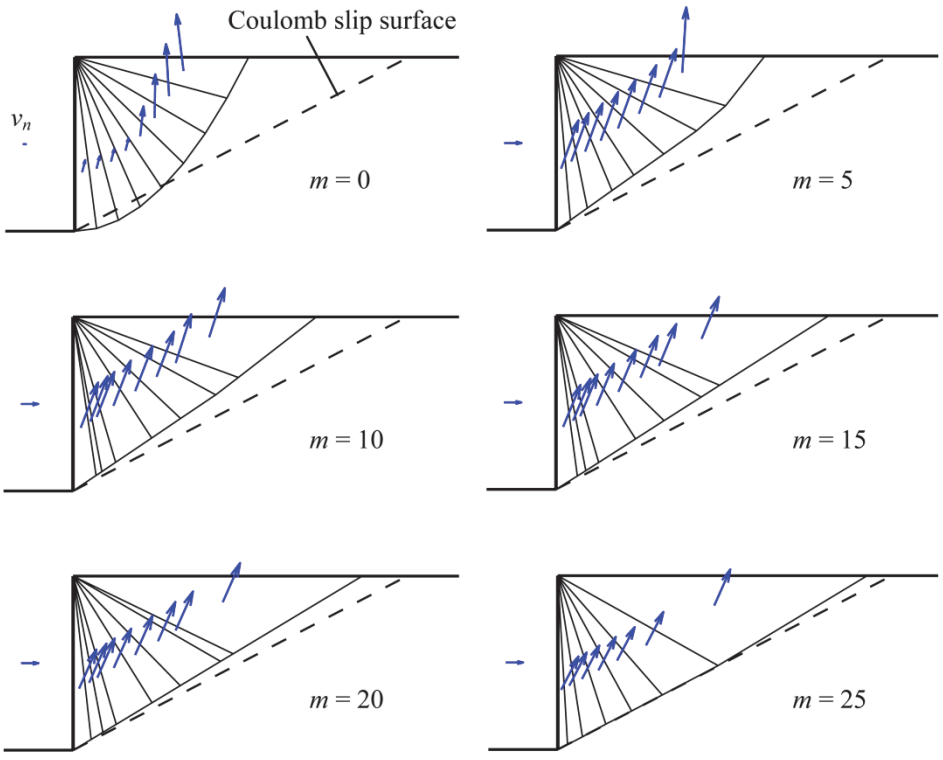

Figure 4. Collapse mechanism for retaining wall at various perturbation steps ($\xi = h$, $N_B = 8$, $\rho_i^1 = 0.04h$, $\phi = 35°$).

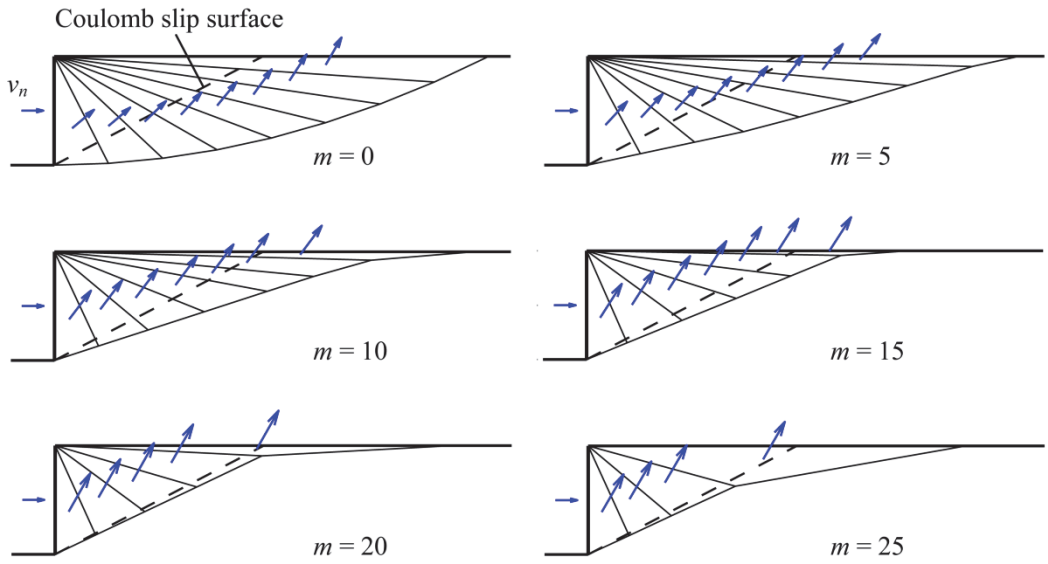

Figure 5. Collapse mechanism for retaining wall at various perturbation steps ($\xi = 4h$, $N_B = 8$, $\rho_i^1 = 0.04h$, $\phi = 35°$).

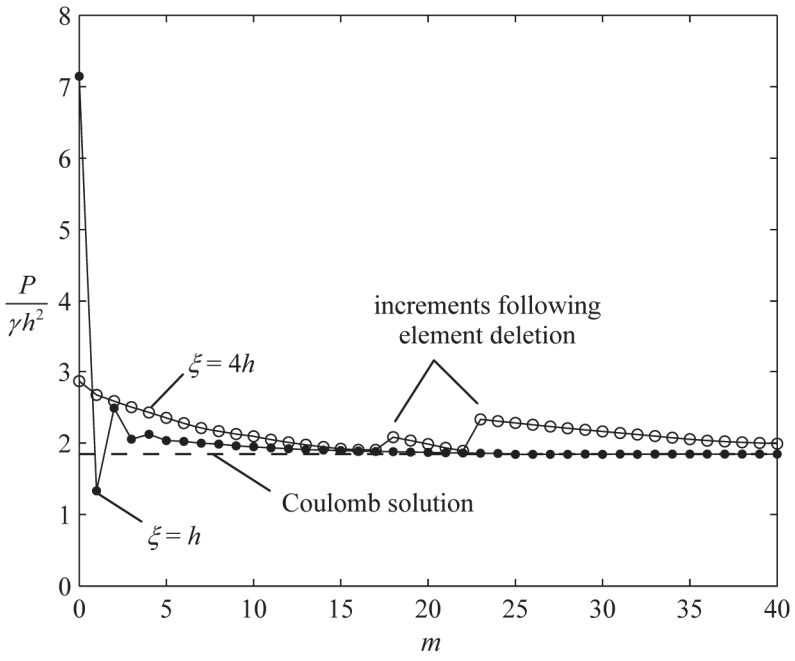

Figure 6. Normalized limit load versus number of perturbation steps for retaining wall example with $\xi = h$ and $\xi = 4h$ ($N_B = 8$ and $\rho_i^1 = 0.04h$).

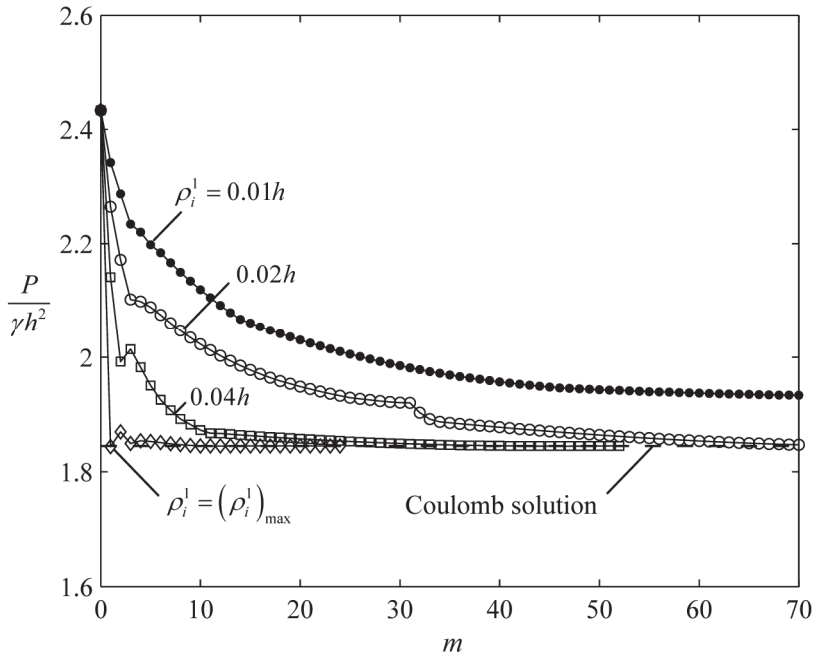

Figure 7. Normalized limit load versus number of perturbation steps for retaining wall example with different values of initial constraint radii ρ_i^1 ($\xi = 2h$, $N_B = 8$, and $\varepsilon = 0.001h$).

Figure 6 shows the variation in the computed limit load, denoted by P, for the cases plotted in Figs. 4 and 5. With $\xi = h$, the computed limit load quickly approaches the true limit load of $P/\gamma h^2 = 1.8451$. In this case, the limit load is initially quite sensitive to the geometry of the mechanism, and a large initial drop can be seen. At step m = 1, the limit load falls below the true one, which is possible in the early perturbation steps on account of the approximate nature of the linearized equations. With ξ = $4h$, jumps in the computed limit load are clearly visible, and these correspond to the block deletions at the surface.

Figure 7 shows the computed limit load at various perturbation steps for $\xi = 2h$, N_B = 8, and several different assumptions for the initial constraint radii ρ_i^1. In each case, the collapse mechanism converges to the Coulomb mechanism, but it clearly does so most rapidly when ρ_i^1 are taken as large as possible, i.e., with $\rho_i^1 = \left(\rho_i^1\right)_{\max}$. For a specified

tolerance of $\varepsilon = 0.001h$, the stopping criterion of Eq. (33) is satisfied at $m = 24$ with $\rho_i^1 = \left(\rho_i^1\right)_{\max}$.

Table 1 summarizes the number of perturbation steps required for convergence, denoted by m^*, and the error between the computed upper bound and the true limit load for various combinations of ξ, ρ_i^1, and ε. It can be seen that m^* is least when $\xi = 2h$, and this is due to the initial collapse mechanism being closest to the optimal one. It also can be seen that the errors in the computed bound are typically quite small. The errors are comparable between $\varepsilon = 0.001h$ and $\varepsilon = 0.0001h$, suggesting an insensitivity to ε provided this tolerance is sufficiently small. For $\varepsilon = 0.01h$, on the other hand, errors can be larger as a result of the stopping criterion being satisfied while the mechanism is still far from optimal.

Table 1. Required number of perturbation steps and absolute error in the computed bound for various choices of ξ, ρ_i^1, and ε in retaining wall example.

ξ	ρ_i^1	$\varepsilon = 0.01h$		$\varepsilon = 0.001h$		$\varepsilon = 0.0001h$	
		m^*	abs. error	m^*	abs. error	m^*	abs. error
h	$0.02h$	25	9.3×10^{-2}	131	8.8×10^{-7}	206	1.2×10^{-6}
	$0.04h$	39	2.1×10^{-6}	71	3.3×10^{-7}	74	3.3×10^{-7}
	$\left(\rho_i^1\right)_{\max}$	35	4.4×10^{-5}	41	9.6×10^{-7}	47	1.5×10^{-7}
$2h$	$0.02h$	18	1.1×10^{-1}	107	6.0×10^{-7}	110	6.1×10^{-7}
	$0.04h$	13	2.0×10^{-2}	52	3.3×10^{-7}	55	3.2×10^{-7}
	$\left(\rho_i^1\right)_{\max}$	21	1.4×10^{-7}	24	1.5×10^{-7}	28	1.5×10^{-7}
$4h$	$0.02h$	119	6.8×10^{-5}	145	5.4×10^{-7}	150	5.2×10^{-7}
	$0.04h$	79	2.9×10^{-7}	159	4.6×10^{-7}	162	4.6×10^{-7}
	$\left(\rho_i^1\right)_{\max}$	61	4.9×10^{-5}	66	5.4×10^{-7}	73	1.3×10^{-7}

Table 2. Required number of perturbation steps and wall-clock times for various choices of N_B in retaining wall example ($\xi = 2h$, $\rho_i^1 = \left(\rho_i^1\right)_{\max}$, and $\varepsilon = 0.001h$).

N_B	m^*	mean wall-clock time per perturbation step (sec)	total wall-clock time (sec)
1	15	0.033	0.50
2	22	0.052	1.15
4	31	0.058	1.79
8	24	0.072	1.73
16	51	0.082	4.18
32	84	0.095	7.97
64	116	0.113	13.10

Table 2 compares m^* and computation times for analyses with varying numbers of blocks. Naturally, the computational effort increases as N_B increases as a result of the larger number of variables, but it also increases due to the larger number of perturbation steps required. The increase in m^* with an increase in N_B can be attributed to the decrease in block size and corresponding reduction in $\left(\rho_i^m\right)_{\max}$, which limits the advances that can be made towards optimizing the mechanism in any given perturbation step. It is seen that the total computation times roughly double as N_B is doubled, but in all cases the analysis was completed in a matter of seconds. Wall-clock times shown in Table 2 were obtained on a computer running Matlab R2010a and Windows 7 (64-bit) with a dual-core 2.67 GHz processor and 8 GB RAM.

4.2. Rough inclined footing

The second example considers the stability of a rough, rigid footing of width b inclined at angle β from the horizontal (see inset in Fig. 8), where $0 \leq \beta \leq 90^\circ$. It is assumed that the

tangential component of velocity for the footing is zero. In this case, shear stresses can develop at the interface between the footing and the soil, but the expression for the unknown normal force at collapse, P, is identical to the one given by Eq. (11). By "rough," it is meant that material directly in contact with the footing moves together with the footing. However, a thin transition zone of deforming material may appear adjacent to the footing surface (segment AC in Fig. 8), and this layer is represented simply as a velocity discontinuity.

Figure 8 shows examples of the two initial arrangements of blocks (N_B = 9 and 104) used as starting guesses for the perturbation method. In both cases, region ABC is initially a triangle whose interior angles are $\angle BAC = \angle ACB = 45^\circ + \phi/2$, and regions CDE and FGA are also triangular with $\angle DCE = \angle CED = \angle GFA = \angle GAF = 45^\circ - \phi/2$. Regions AGB and CBD are bounded by log spirals. Adaptations to these initial configurations were required for large values of β, since region CBD vanishes as β approaches 90°, but the assumed geometry remained similar to that shown in Fig. 8. As motivated by results from the previous example (Section 4.1), parameters used in the analysis were $\rho_i^1 = \left(\rho_i^1\right)_{\max}$ and $\varepsilon = 0.001b$.

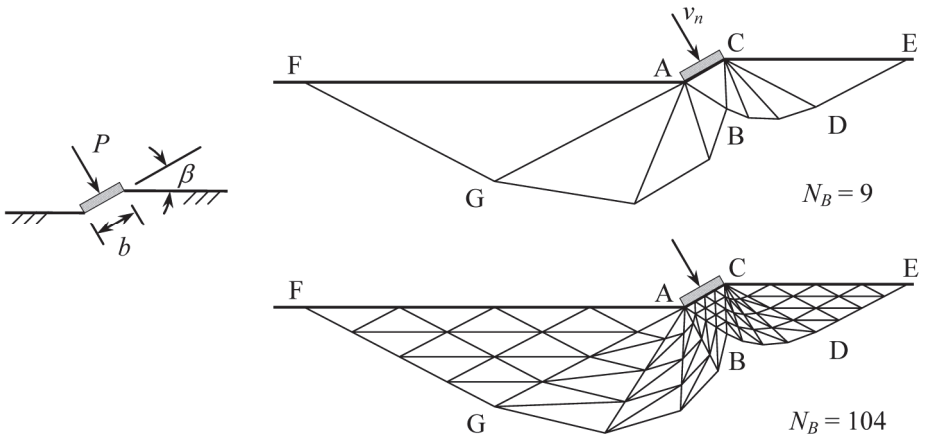

Figure 8. Initial arrangements of rigid blocks used to analyze a rough inclined footing (examples shown are for $\beta = 30°$ and $\phi = 35°$).

Figure 9 shows the optimal collapse mechanisms ($m = m^*$) computed using the perturbation method for $\beta = 30°$, $\phi = 0$, and $\gamma b/c = 1$. Clearly, the optimal mechanisms obtained with $N_B = 9$ and $N_B = 104$ are similar in character, and this was also the case for other values of β, c, ϕ, and γ.

Figure 10 gives the optimal collapse mechanisms for purely cohesive material ($\phi = 0$) and several combinations of inclination angle β and normalized unit weight $\gamma b/c$. For clarity, only the mechanisms for $N_B = 9$ are plotted. With weightless material ($\gamma b/c = 0$), it is seen that material flows only toward the front of the footing (boundary CE in Fig. 8) and there is relative sliding between the footing and the underlying material. For $\gamma b/c = 5$, material flows to both the front and back of the footing, and there is no relative sliding. All mechanisms in Fig. 10 were easily distinguished and optimized using the perturbation method. For mechanisms with only forward flow of material (e.g. $\gamma b/c = 0$ and $\beta = 30°$), velocities were zero in the optimized mechanism for blocks in regions FGA and AGD, and these blocks are not plotted in the figures.

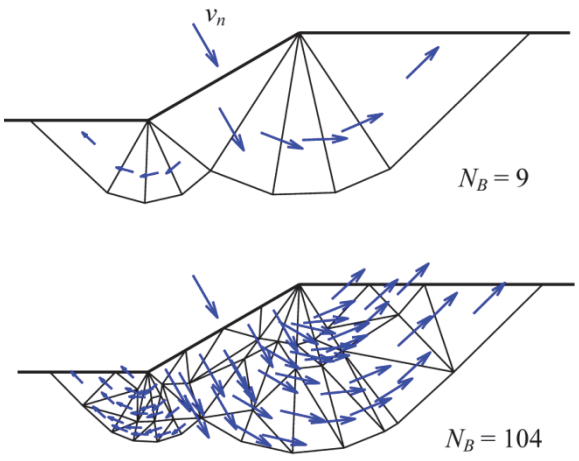

Figure 9. Optimal collapse mechanisms for rough inclined footing with $\beta = 30°$, $\phi = 0$, and $\gamma b/c = 1$.

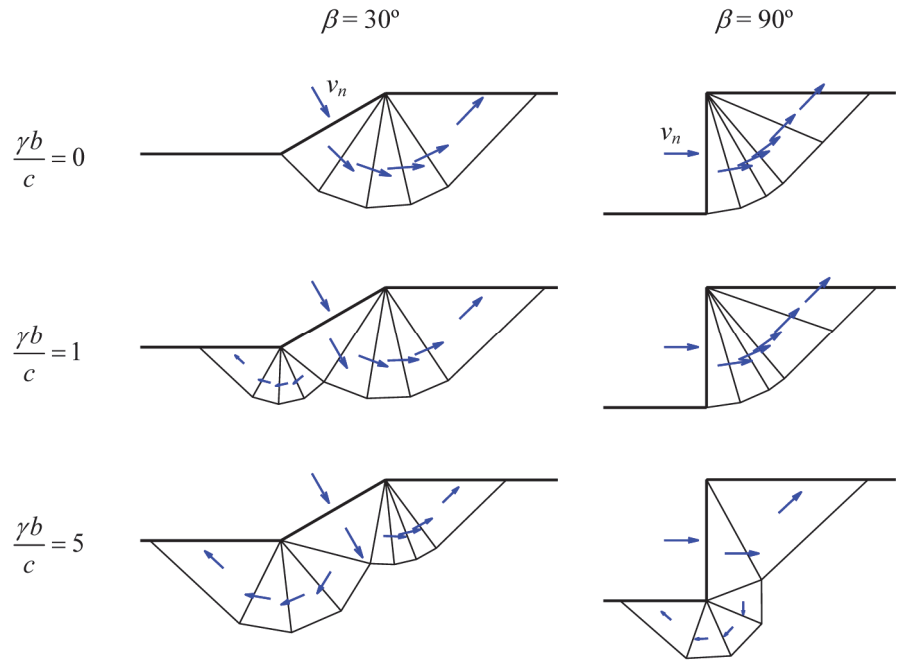

Figure 10. Optimal collapse mechanisms with $\phi = 0$ and different combinations of β and normalized unit weight $\gamma b/c$ ($N_B = 9$; blocks with zero velocity are omitted for clarity).

Table 3. Upper bounds on limit load for rough inclined footing with $\phi = 0$.

β (deg)	P/cb					
	$N_B = 9$			$N_B = 104$		
	$\gamma b/c = 0$	$\gamma b/c = 1$	$\gamma b/c = 5$	$\gamma b/c = 0$	$\gamma b/c = 1$	$\gamma b/c = 5$
0	5.19	5.20	5.20	5.18	5.18	5.18
10	5.13	5.16	5.19	5.13	5.15	5.18
20	4.96	5.05	5.20	4.93	5.03	5.18
30	4.73	4.89	5.21	4.68	4.87	5.18
40	4.36	4.68	5.22	4.33	4.64	5.19
50	4.00	4.38	5.25	3.98	4.36	5.20
60	3.64	4.07	5.26	3.62	4.06	5.22
70	3.30	3.75	5.25	3.27	3.74	5.20
80	2.93	3.42	5.18	2.92	3.42	5.15
90	2.58	3.08	5.01	2.57	3.07	4.98

Table 3 gives the computed upper bounds on the normalized limit load for purely cohesive material ($\phi = 0$). The difference in the bounds computed with $N_B = 9$ and $N_B = 104$ is quite small in all cases, suggesting that a reasonable level of accuracy is achieved with only a few blocks. For the case of weightless material ($\gamma b/c = 0$), Fig. 11 compares the bounds computed with $N_B = 104$ with results available in the literature. With $\beta = 0$, the computed bound is very close to the exact value determined by Prandtl [30] using the method of characteristics. For large values of β, one can assume that relative sliding occurs and construct a solution similar to the one by Grunzweig, *et al.* [31] using the method of characteristics. This solution is also plotted in Fig. 11, and very good agreement with the computed upper bounds can be seen.

Computed upper bounds for purely frictional material with $\phi = 35^\circ$ are given in Table 4. Unlike the case $\phi = 0$, the numerical results are sensitive to the number of blocks N_B, particularly for small values of β. With $\beta = 0$, for example, the configuration is identical to the challenging "N_γ problem" discussed at length in the literature (e.g. [3, 32-34]), and the computed upper bound decreases by 22% as N_B changes from 9 to 104. To further investigate the performance of the method for this benchmark problem, additional analyses that took advantage of symmetry and allowed for variable N_B were conducted. The computed upper bounds are shown in Table 5, where it is seen that the numerical results approach the true limit load of $P/\gamma b^2 = 17.238$ determined by Martin [34]. Also shown are the wall-clock times required for the simulations, which become sizeable as N_B is made very large.

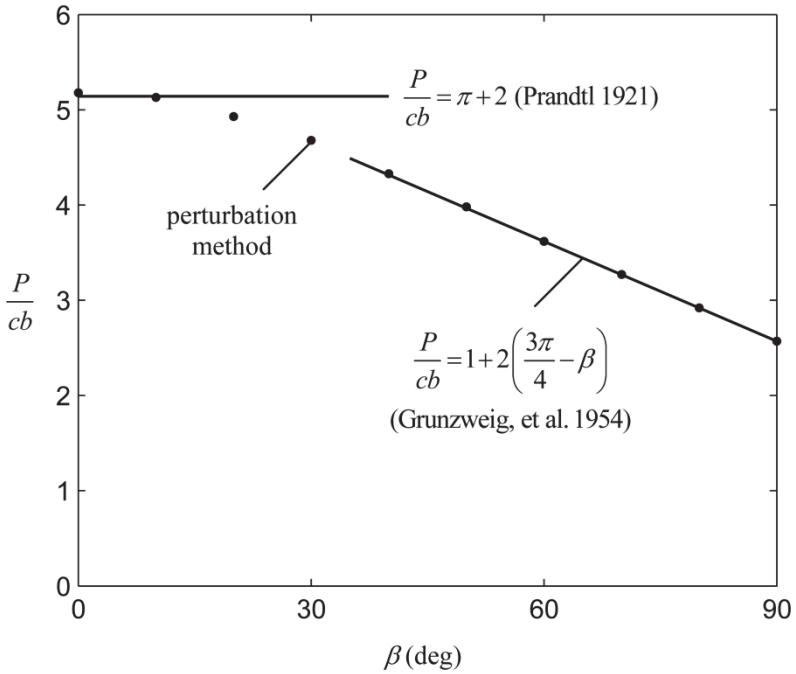

Figure 11. Limit load versus footing inclination angle for rough footing on purely cohesive, weightless material ($\phi = 0$, $\gamma b/c = 0$, $N_B = 104$).

Table 4. Computed upper bounds for rough inclined footing with $c = 0$ and $\phi = 35°$.

β (deg)	$\frac{P}{\gamma b^2}$	
	$N_B = 9$	$N_B = 104$
0	26.9	20.8
10	26.3	20.2
20	24.4	18.9
30	21.6	17.4
40	18.2	14.9
50	14.7	12.6
60	13.0	11.3
70	9.19	8.26
80	6.52	6.01
90	4.64	4.38

Table 5. Computed upper bounds for $c = 0$, $\phi = 35°$, and $\beta = 0$ (N_γ problem) based on symmetric analysis with variable N_B.

N_B	$\frac{P}{\gamma b^2}$	m^*	% difference from Martin (2005)	mean wall-clock time per perturbation step (sec)	total wall-clock time (sec)
13	25.2	159	46.4	0.23	37
54	21.0	147	21.5	0.61	90
220	19.2	35	11.4	5.65	198
888	18.4	95	6.5	143.2	13,605

4.3. Rectangular block on a rough surface

As a final example, we consider the stability of a rectangular block of purely cohesive material ($\phi = 0$) resting on a rough surface, where the term "rough" carries the same meaning as discussed in Section 4.2. The height and width of the block are denoted by h and b, respectively, and the unit weight of the material is viewed as the load inducing collapse (see inset in Fig. 12). Aspect ratios considered in the analysis are h/b = 1/4, 1/2, 1, 2, and 4, and parameters for the perturbation method are taken as $\rho_i^1 = \left(\rho_i^1\right)_{\max}$ and $\varepsilon = 0.001b$. Examples of the assumed initial block arrangements and computed initial velocities ($m = 0$) are given in Figs. 12 and 13. Blocks were initially placed in groups of four to construct square units, and the lengths of these square units were $h/4$ for $h/b < 1/2$ and $b/4$ for $h/b \geq 1/2$.

Figures 12 and 13 depict the optimal mechanisms as obtained using the perturbation method ($m = m^*$) for h/b = 1/2 and 2, respectively. For h/b = 1/2, the mechanism is confined to a fraction of the block's width, and it is effectively the same as that for a vertical cut, as considered by Pastor, et al. [35] and Lyamin and Sloan [15]. For h/b = 2, the mechanism spans the entire width of the block. In both cases, the mechanism is initially symmetric but

becomes non-symmetric as the mechanism is perturbed. The tendency for the perturbation method to produce a non-symmetric final mechanism can be attributed to the high probability that symmetry is lost during the numerous intermediate perturbation steps. It should be noted, however, that a non-symmetric mechanism may in this case furnish a limit load that is very close or even the same as the optimal symmetric mechanism. In other words, the mechanism corresponding to the true limit load may be non-unique, as in other well-known stability problems.

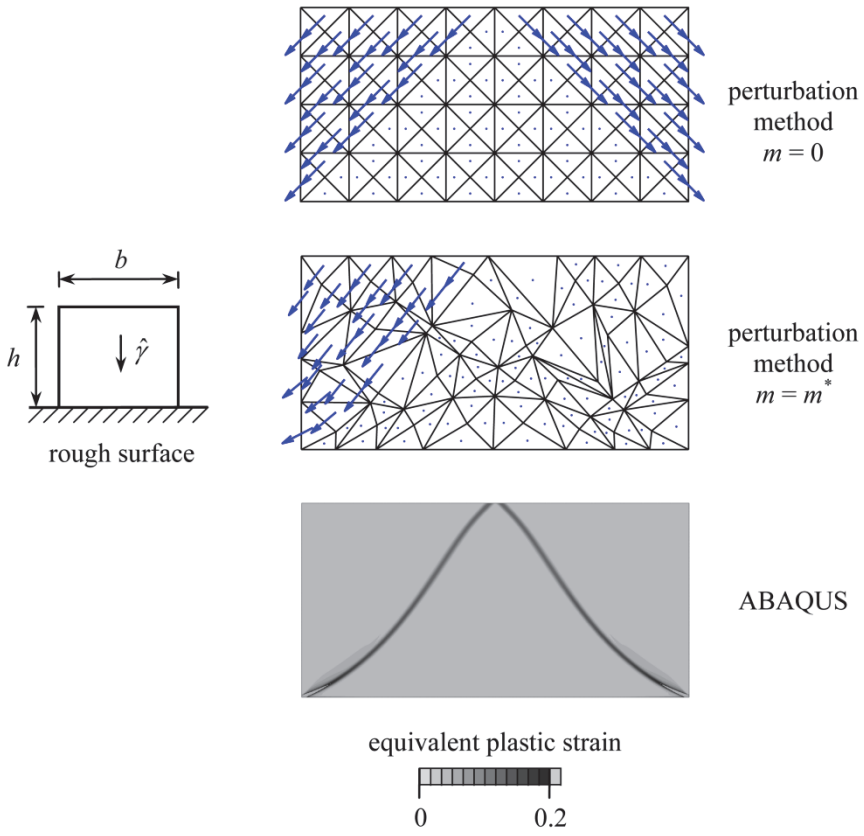

Figure 12. Collapse mechanisms for block on a rough surface ($h/b = 1/2$).

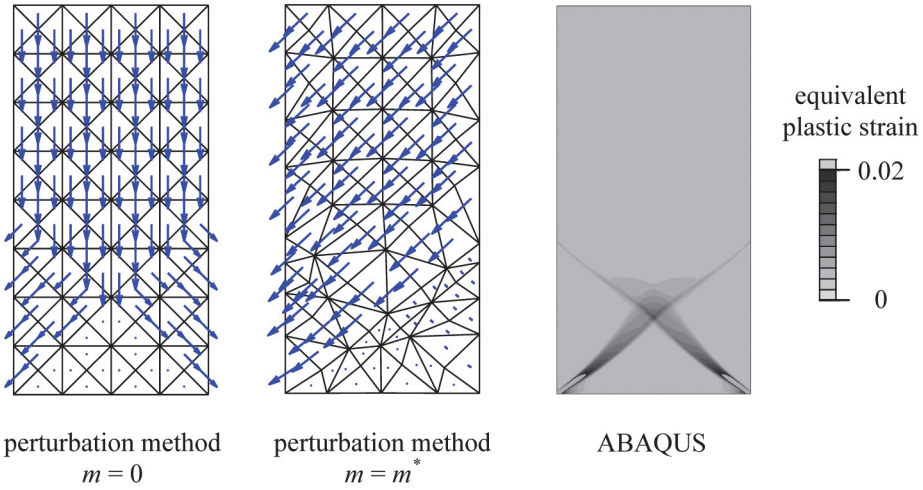

Figure 13. Collapse mechanisms for block on a rough surface ($h/b = 2$).

For comparison, the mechanisms evaluated using the perturbation method are plotted together with the strain fields obtained from finite element simulations using ABAQUS. In these simulations, the material was assumed to be elastic-perfectly plastic (Young's modulus = $1000c$; Poisson's ratio = 0.49), and material representing the block was discretized using reduced integration quadrilateral elements with edge lengths of $h/128$ for $h/b < 1/2$ and $b/128$ for $h/b \geq 1/2$. Simulations were performed by increasing the value of unit weight until the code failed to converge, at which point the applied unit weight corresponds to the collapse load. The plots of equivalent plastic strain from ABAQUS, shown in Figs. 12 and 13, confirm that deformation is primarily in the form of thin, curved bands emanating from the lower corners of the block. Unlike the collapse mechanisms evaluated using the perturbation method, the deformation is symmetric in the finite element simulations. Despite this basic difference, the dominant velocity jumps predicted using the perturbation method coincide with zones of concentrated deformation in the finite element simulations.

Table 6. Normalized unit weight at collapse for block on a rough surface.

$\frac{h}{b}$	$\frac{\hat{\gamma}h}{c}$	
	perturbation method	ABAQUS
0.25	3.79	3.78
0.5	3.81	3.78
1	3.22	3.12
2	2.55	2.54
4	2.26	2.26

Computed upper bounds on the normalized unit weight at collapse, $\hat{\gamma}h/c$, are given in Table 6. With h/b = 1/4 and 1/2, the upper bounds evaluated using the perturbation method are very close to the upper bound of $\hat{\gamma}h/c = 3.786$ evaluated by Pastor, et al. [35] for a vertical cut. Very good agreement with the collapse loads determined using ABAQUS can also be observed for all values of h/b, with the collapse loads from ABAQUS being slightly lower than the upper bounds computed using the perturbation method.

5. Discussion

In each of the examples considered in Section 4, the perturbation method converged to a mechanism for which the computed upper bound was close to the true limit load. In general, however, there is no assurance that the method always converges, and although the computed limit load is a rigorous upper bound, it is not necessarily the global optimum. Whether or not the method converges to the global optimum depends strongly on the assumed initial arrangement of blocks and, to some extent, parameters affecting the progression of

perturbation steps (e.g., ρ_i^m). The dependence on the initial arrangement closely parallels the mesh-dependence of standard FELA and grid-dependence of DLO. Efficient implementation of DLO, for example, requires a starting guess in the form of an assumed partial node connectivity [24].

In total, the proposed perturbation method requires three different types of input: (1) an initial arrangement of blocks, (2) a set of initial constraint radii $\rho_i^1 \leq \left(\rho_i^1\right)_{\max}$, and (3) the tolerance ε representing a threshold for the final constraint radii. The initial arrangement of blocks can take many forms, ranging from the problem-specific type utilized in the examples of Sections 4.1 and 4.2 to the structured "mesh" considered in the example of Section 4.3. It is unknown whether a systematic approach for generating the initial arrangement of blocks can be developed, and this represents a potential area of future research.

Numerical results from Section 4.1 suggest that the optimal limit load is determined in fewest number of perturbation steps when the initial constraint radii ρ_i^1 are taken as large as possible. It should be noted, however, that the iterative perturbation procedure described in Section 3.2 is *ad hoc*, and the procedure is adopted primarily for its simplicity. The development of new and improved strategies for iteration represents another possible subject for future study.

The stopping criterion of Eq. (33) was established with a view towards precisely determining the optimal geometry of the collapse mechanism. On the other hand, as seen in Section 4.1, reasonable estimates of the limit load are typically achieved in far fewer perturbation steps than that required to satisfy Eq. (33). If the mechanism itself is deemed of secondary importance, greater efficiency can be achieved by expressing the stopping criterion in terms of the limit load, as suggested by Johnson [26].

6. Conclusions

The paper presents a numerical technique for computing rigorous bounds on limit loads through optimization of rigid block mechanisms consisting of an arbitrary number of sliding triangular blocks. The method is premised on determining the optimal collapse mechanism through multiple successive perturbations, where the optimization problem corresponding to each perturbation step is solved using second-order cone programming. As compared to similar concepts presented in previous works [25, 26], the proposed technique is straightforward to implement, and its novel features include the problem formulation within each perturbation step, the iterative perturbation procedure, and the inclusion of material self-weight. The method represents a valuable alternative to the analytical method of limit analysis described in Section 1, and it is likely that the approach can be extended to traditional FELA in which velocities vary continuously within elements. The perturbation concept also may have application in refining mechanisms determined using DLO, where velocity discontinuities are otherwise restricted to a specified grid. Though plane strain was assumed in this paper, a three dimensional formulation should be possible. In three dimensions, the perturbation technique may prove to be particuarly effective as compared to existing approaches, where the extension from two to three dimensions can be arduous.

Acknowledgement

Financial support for this research was provided by the Australian Research Council (grant number FL0992039) in the form of an Australian Laureate Fellowship awarded to Professor Scott Sloan.

Appendix A: Upper limit on constraint radius

In this appendix we evaluate an upper limit on the distance that the vertices of a triangular block can move without risk of the block inverting ($A_j < 0$ in Eq. (6)). We first consider a single block for which each vertex is constrained by the same radius, and this result is then used to arrive at an upper limit for a vertex within an arrangement of blocks.

Figure 14(a) gives a geometric representation of radial constraints imposed on the vertices of a single triangular block, where the vertices are represented as points *A*, *B*, and *C*. For the area of the block to become exactly zero within a perturbation step, the vertices of the block must become co-linear, and this is possible only if there exist one or more lines that pass through all three circles corresponding to the radial constraints. The upper limit on the constraint radius, denoted ρ, is therefore determined by the limit in which any line that passes through each circle is also tangent to each circle. Figure 14(a) is drawn for this scenario, where tangent line *EF* is the only line passing through all three circles. Since the constraint radii at all vertices are equal by assumption, line *EF* bisects the altitude *AD*, and the value of ρ can be readily computed as

$$\rho = \frac{h_A}{2} \tag{34}$$

where h_A is the length of the altitude passing through point *A*. The length of this altitude, as well as the altitudes passing through points *B* and *C*, are given by

$$h_A = \frac{l_B l_C}{2R}, \quad h_B = \frac{l_A l_C}{2R}, \quad h_C = \frac{l_A l_B}{2R} \tag{35}$$

where l_A, l_B, and l_C are the lengths of the edges opposing points A, B, and C, respectively, and R is the circumradius of the triangle, computed as

$$R = \frac{l_A l_B l_C}{\sqrt{(l_A + l_B + l_C)(l_B + l_C - l_A)(l_C + l_A - l_B)(l_A + l_B - l_C)}} \tag{36}$$

Without loss of generality, we assume that $l_A \geq l_B \geq l_C$, and it follows from Eq. (35) that $h_A \leq h_B \leq h_C$. Using the fact that h_A is the smallest altitude, it can be shown Eq. (34) is sufficient to ensure that any line passing through each circle in Fig. 14(a) is also tangent to each circle, and thus Eq. (34) also suffices to ensure the area of the block does not become negative within a perturbation step.

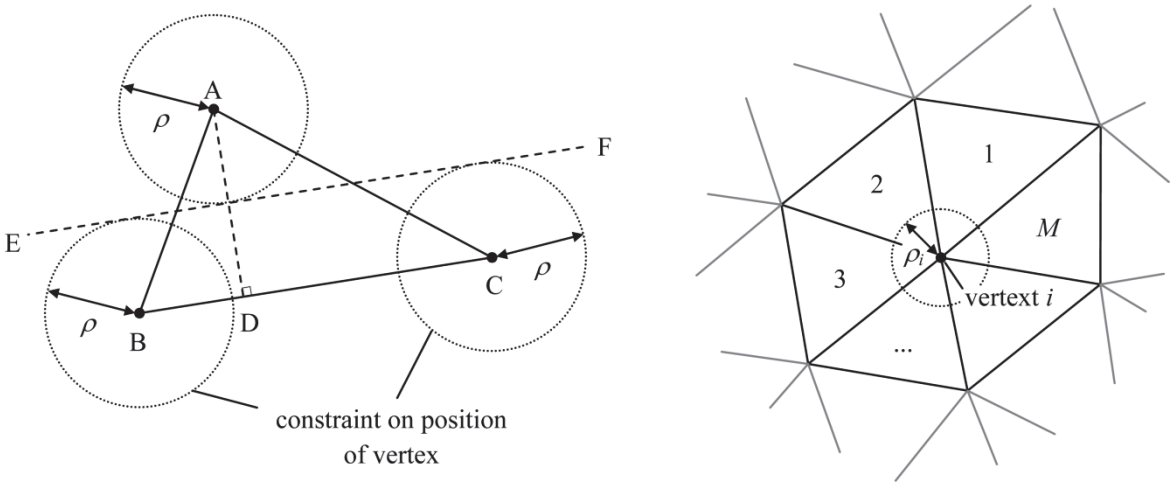

Figure 14. Radial constraints on positions of vertices for (a) a single block and (b) multiple blocks in an assembly.

For a single vertex belonging to multiple blocks in an arrangement, as illustrated in Fig. 15(b), no blocks will not invert if the constraint radius for the vertex is selected as the smallest value of ρ from all blocks sharing the vertex. Using $\left(\rho_i^m\right)_{\max}$ to denote the maximum constraint radius for vertex *i* in perturbation step *m*, we may write

$$\left(\rho_i^m\right)_{\max} = \frac{1}{2}\min\left\{h_A^1, h_B^1, h_C^1, h_A^2, h_B^2, h_C^2, \ldots, h_A^M, h_B^M, h_C^M\right\} \tag{37}$$

where superscripts indicate the blocks to which vertex *i* belongs (see Fig. 15(b)). Equation (37) has been expressed so as to be independent of any assumption regarding the relative lengths of the blocks' edges, and this allows for Eqs. (35) and (36) to be used directly for evaluating h_A, h_B, and h_C.

Appendix B: Block deletions

In this paper, we adopt the following criterion for identifying blocks that should be deleted

$$\frac{\rho_I}{\rho_{II}} < \varepsilon_{del} \tag{37}$$

where ρ_I and ρ_{II} are values of the constraint radii for any two adjacent blocks (computed as in Appendix A) and ε_{del} is a specified tolerance. With the aid of Eq. (34), Eq. (37) may be equivalently written as

$$\frac{h_I}{h_{II}} < \varepsilon_{del} \tag{38}$$

where h_I and h_{II} are the minimum altitudes in adjacent blocks.

Upon detecting a pair of blocks for which the criterion of Eq. (37) or (38) is satisfied, the block with the smaller minimum altitude (h_I) is deleted. This is achieved in the following steps, where comments in parentheses refer to Fig. 15:

1. Identify the vertex corresponding to the minimum altitude in the block to be deleted (vertex A).
2. Identify the shortest edge in the block to be deleted (edge AC).
3. Identify the second vertex (i.e. not the one from step (1)) for the edge found in step (2) (vertex C).
4. Identify the block that shares the edge found in step (2) (block ACE).
5. Delete the block found in step (3) and the block originally detected for deletion (blocks ACE and ABC).
6. Re-establish the vertex from step (3) (vertex C) as the new vertex for all blocks originally containing the vertex from step (1) (blocks AGB, BFG, and ACE).

The final configuration after block deletion is also shown in Fig. 16. It should be noted that a slightly different procedure is necessary for blocks on boundaries, but the process can be easily extended to handle these cases.

Through trial and error, a threshold of $\varepsilon_{del} = 0.1$ was found to be suitable for most problems. This value was assumed for all results presented in this paper.

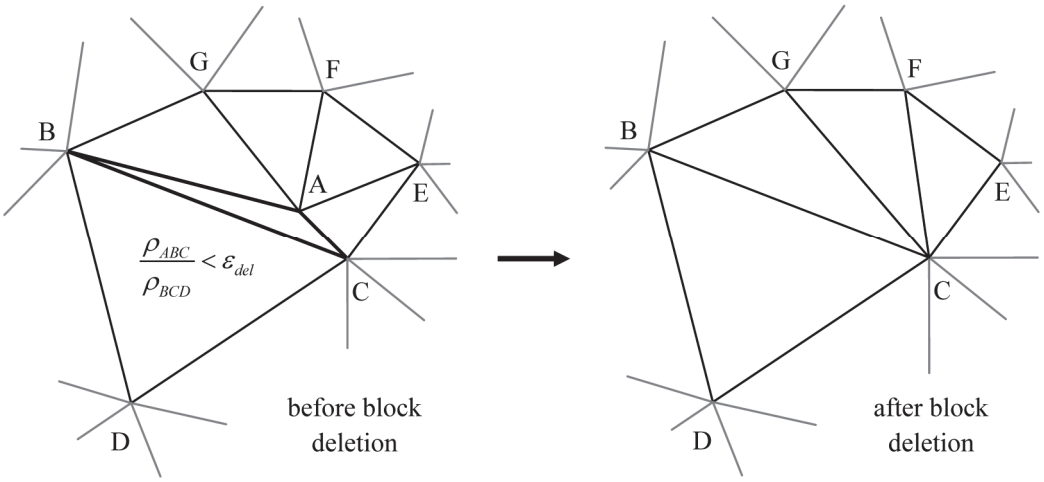

Figure 15. Arrangement of blocks before and after deletion of block ABC.

References

[1] Chen W-F. Limit analysis and soil plasticity. Amsterdam: Elsevier; 1975.

[2] Michalowski RL. Slope stability analysis: a kinematical approach. Géotechnique. 1995;45(2):283-93.

[3] Michalowski RL. An estimate of the influence of soil weight on bearing capacity using limit analysis. Soils Found. 1997;37(4):57-64.

[4] Michalowski RL. Displacements of multiblock geotechnical structures subjected to seismic excitation. J Geotech Geoenviron Eng. 2007;133(11):1432-9.

[5] Puzrin AM, Randolph MF. New planar velocity fields for upper bound limit analysis. Int J Solids Struct. 2003;40(13-14):3603-19.

[6] Kumar J, Ghosh P. Upper bound limit analysis for finding interference effect of two nearby strip footings on sand. Geotech Geol Eng. 2007;25(5):499-507.

[7] Michalowski RL, Drescher A. Three-dimensional stability of slopes and excavations. Géotechnique. 2009;59(10):839-50.

[8] Georgiadis K. An upper-bound solution for the undrained bearing capacity of strip footings at the top of a slope. Géotechnique. 2010;60(10):801-6.

[9] Hambleton JP, Drescher A. Approximate model for blunt objects indenting cohesive-frictional materials. Int J Numer Anal Methods Geomech. 2011;36(3):249-71.

[10] Yamamoto K, Lyamin AV, Wilson DW, Sloan SW, Abbo AJ. Bearing capacity of cohesive-frictional soils with a shallow square tunnel. Can Geotech J. 2011;48(12):1841-54.

[11] Anderheggen E, Knöpfel H. Finite element limit analysis using linear programming. Int J Solids Struct. 1972;8(12):1413-31.

[12] Bottero A, Negre R, Pastor J, Turgeman S. Finite element method and limit analysis theory for soil mechanics problems. Comput Methods Appl Mech Eng. 1980;22(1):131-49.

[13] Sloan SW. Upper bound limit analysis using finite elements and linear programming. Int J Numer Anal Methods Geomech. 1989;13(3):263-82.

[14] Sloan SW, Kleeman PW. Upper bound limit analysis using discontinuous velocity fields. Comput Methods Appl Mech Eng. 1995;127(1-4):293-314.

[15] Lyamin AV, Sloan SW. Upper bound limit analysis using linear finite elements and non-linear programming. Int J Numer Anal Methods Geomech. 2002;26(2):181-216.

[16] Krabbenhoft K, Lyamin AV, Hjiaj M, Sloan SW. A new discontinuous upper bound limit analysis formulation. Int J Numer Meth Eng. 2005;63(7):1069-88.

[17] Makrodimopoulos A, Martin CM. Upper bound limit analysis using simplex strain elements and second-order cone programming. Int J Numer Anal Methods Geomech. 2007;31(6):835-65.

[18] Makrodimopoulos A, Martin CM. Upper bound limit analysis using discontinuous quadratic displacement fields. Commun Numer Methods Eng. 2008;24(11):911-27.

[19] Zhang X, Qian L. Rigid finite element and limit analysis. Acta Mechanica Sinica. 1993;9(2):156-62.

[20] Zhang X. Slope stability analysis based on the rigid finite element method. Géotechnique. 1999;49(5):585-93.

[21] Chen J, Yin J-H, Lee CF. Upper bound limit analysis of slope stability using rigid finite elements and nonlinear programming. Can Geotech J. 2003;40(4):742-52.

[22] Orduña A, Lourenço PB. Three-dimensional limit analysis of rigid blocks assemblages. Part I: Torsion failure on frictional interfaces and limit analysis formulation. Int J Solids Struct. 2005;42(18-19):5140-60.

[23] Borges L, Zouain N, Costa C, Feijóo R. An adaptive approach to limit analysis. Int J Solids Struct. 2001;38(10-13):1707-20.

[24] Smith CS, Gilbert M. Application of discontinuity layout optimization to plane plasticity problems. Proc Royal Soc A. 2007;463(2086):2461-84.

[25] Milani G, Lourenço PB. A discontinuous quasi-upper bound limit analysis approach with sequential linear programming mesh adaptation. Int J Mech Sci. 2009;51(1):89-104.

[26] Johnson D. Yield-line analysis by sequential linear programming. Int J Solids Struct. 1995;32(10):1395-404.

[27] Hambleton JP, Sloan SW. Coordinate perturbation method for upper bound limit analysis. In: Pande GN, Pietruszczak S, editors. 2nd International Symposium on Computational Geomechanics. Dubrovnik; 2011. 373-84.

[28] Lyamin AV, Krabbenhøft K, Hjiaj M, Sloan SW. Discontinuous velocity field for general yield criteria. In: Pande G, Pietruszczak S, editors. Numerical Models in Geomechanics-NUMOG IX. Ottawa; 2004. 291-6.

[29] Sturm JF. Using SeDuMi 1.02, A Matlab toolbox for optimization over symmetric cones. Optim Methods Soft. 1999;11(1):625-53.

[30] Prandtl L. Über die Eindringungsfestigkeit (Härte) plastischer Baustoffe und die Festigkeit von Schneiden. Zeitschrift für angewandte Mathematik und Mechanik. 1921;1(1):15-20.

[31] Grunzweig J, Longman IM, Petch NJ. Calculations and measurements on wedge-indentation. J Mech Phys Solids. 1954;2(2):81-6.

[32] Meyerhof GG. Ultimate bearing capacity of foundations. Géotechnique. 1951;2(4):301-30.

[33] Hjiaj M, Lyamin AV, Sloan SW. Numerical limit analysis solutions for the bearing capacity factor N. Int J Solids Struct. 2005;42(5-6):1681-704.

[34] Martin CM. Exact bearing capacity calculations using the method of characteristics. Proceedings of the 11th International Conference of IACMAG. Torino; 2005.

[35] Pastor J, Thai TH, Francescato P. New bounds for the height limit of a vertical slope. Int J Numer Anal Methods Geomech. 2000;24(2):165-82.